# Competition of two distinct actin networks for actin defines a bistable switch for cell polarization

**Alexis J. Lomakin**[1,2,*,†], **Kun-Chun Lee**[3,*,†], **Sangyoon J. Han**[1,†], **D A. Bui**[1], **Michael Davidson**[4], **Alex Mogilner**[3,†], and **Gaudenz Danuser**[1,†]

[1]Department of Cell Biology, Harvard Medical School, 240 Longwood Avenue, Boston, Massachusetts 02115, USA

[2]Department of Microbiology & Immunobiology, Harvard Medical School, 77 Avenue Louis Pasteur, Boston, Massachusetts 02115, USA

[3]Department of Neurobiology, Physiology and Behavior and Department of Mathematics, University of California, Davis, 1 Shields Avenue, Davis, California 95616, USA

[4]National High Magnetic Field Laboratory and Department of Biological Science, Florida State University, 1800 E. Paul Dirac Drive, Tallahassee, Florida 32310, USA

## Abstract

Symmetry-breaking polarization enables functional plasticity of cells and tissues and is yet not well understood. Here we show that epithelial cells, hard-wired to maintain a static morphology and to preserve tissue organization, can spontaneously switch to a migratory polarized phenotype upon relaxation of the actomyosin cytoskeleton. We find that myosin-II engages actin in the formation of cortical actomyosin bundles and thus makes it unavailable for deployment in the process of dendritic growth normally driving cell motility. At low contractility regimes epithelial cells polarize in a front-back manner due to emergence of actin retrograde flows powered by dendritic polymerization of actin. Coupled to cell movement, the flows transport myosin-II from the front to the back of the cell, where the motor locally "locks" actin in contractile bundles. This polarization mechanism could be employed by embryonic and cancer epithelial cells in microenvironments where high contractility-driven cell motion is inefficient.

---

## Introduction

The inherent ability of some animal cell types to easily change shape and initiate polarized movements reflects their functional requirement to explore the space around them. On the other end of the spectrum are cell types, particularly differentiated ones such as epithelial cells, which maintain a static morphology to preserve tissue organization and function. However, during embryo- and carcinogenesis epithelial cells can spontaneously lose their organization and acquire anteroposterior polarity characteristic of mesenchymal cells[1]. The cell shape changes are prerequisites for directional cell migration and adaptation to variable microenvironments. Characteristic molecular circuits regulating the epithelial cell morphodynamics involve members of the Rho family of small GTPases, which communicate polarity information to the actin cytoskeleton[2–4]. In tumor epithelial cells, RhoA GTPase stimulates actomyosin contractility, which rounds-up the cell, while Rac1 GTPase excites actin polymerization to enable the formation of polarized cell protrusions[5]. The two GTPases inhibit each other through intermediate biochemical reactions, and this reciprocal inhibitory cross-talk is predicted to effectively increase the signal gain in favor of either specific Rho-type or Rac-type cell morphologies[6]. A challenge in testing this model is that many of the molecular factors mediating the inhibitory cross-talk have not been identified[7]. Moreover, the key events underlying large-scale cell reorganization upon signal gain in favor of a specific GTPase are unknown. Therefore, in the present study, we set out to determine the fundamental organizing principles that link molecular activities of signaling systems to cell polarization.

## Results

### Myosin-II inhibits spontaneous symmetry breaking and motility initiation in epithelial cells

To understand how epithelial cells maintain and break their normal morphology, we performed experiments aimed at identifying a regulatory switch that excites cell shape polarization upon turning ON or OFF the activity of signaling circuits controlled by Rho GTPases. We analyzed the degree of structural polarity in single non-tumorigenic rat liver epithelial cells IAR-2 in different signaling states. Among the conserved Cdc42-, RhoA-, and Rac1-mediated polarity pathways, the signaling cascade RhoA → Rho-kinase (ROCK) → myosin-II regulatory light chain (MRLC) emerged as a unique molecular circuit whose attenuation transforms non-polarized cells into polarized ones (Supplementary Fig. 1a, b). Since the cascade terminates at the motor protein myosin-II (further referred to as myosin), we directly ablated its ATPase activity with the small-molecule drug blebbistatin (BBS, 25 μM). When allowed to spread on a glass surface, IAR-2 cells assumed a discoid shape with almost perfect circular symmetry, which they maintained over hours (Fig. 1 and Supplementary Video 1). However, after addition of BBS, the cells underwent a spontaneous large-scale reorganization manifested in migratory polarization (Fig. 1a, b, Supplementary Fig. 1c, d and Supplementary Video 2): cells pushed their prospective front out and pulled in the back end, followed by initiation of persistent whole-cell migration (Fig. 1a–c and Supplementary Video 3). Polarization was stable in the presence of BBS (Fig. 1b, red curve), but cells switched back to their original, circularly symmetric shapes upon wash

out of BBS (Supplementary Fig. 2), indicating that myosin activity is the mediator of a reversible polarization switch.

Acute inhibition of RhoA and ROCK, but not other potentially involved molecular factors, produced a phenotypic response remarkably similar to BBS treatment (Supplementary Fig. 1c, d), suggesting that myosin activity plays a decisive role in controlling large-scale morphodynamics of epithelial cells. To exclude non-specific effects of the small molecule inhibitors, we separately depleted by siRNA-mediated gene silencing the two major isoforms of the myosin heavy chain, myosin-IIA and myosin-IIB. As partially expected from previous studies[8, 9], knock-down of myosin-IIA, but not of myosin-IIB, resulted in the phenotype of epithelial cells treated with BBS (Supplementary Fig. 3a–d). Indeed, we succeeded in rescuing the myosin-IIA deficiency phenotype in IAR-2 cells by ectopic expression of RNAi-insensitive ATPase-competent wild-type myosin-IIA, while expression of the RNAi-insensitive ATPase-defective mutant myosin-IIA (N93K27)[10] did not rescue the phenotype (Supplementary Fig. 3e). This rules out mechanisms other than myosin ATPase activity to control migratory polarization of epithelial cells, and justifies the use of the myosin ATPase inhibitor BBS as a specific tool to modulate migratory cell polarization.

## Integrin-based substrate anchorage does not explain the inhibition of migratory cell polarization by myosin-II in epithelial cells

Myosin activity promotes growth of integrin-based focal adhesions (FA) attaching cells to the extracellular matrix (ECM)[11]. Strong anchorage of cells to ECM *via* FAs renders cells immobile[12, 13]. At the same time, there are cases when cells can initiate motility upon direct weakening of FAs[14, 15]. We thus hypothesized that myosin in epithelial cells prevents migratory cell polarization by facilitating strong FA-mediated attachment to ECM. However, our analyses of cell morphology as well as motility initiation frequency in cells plated on various adhesive and non-adhesive substrates did not support this hypothesis (Fig. 2), calling for an alternative explanation of myosin's effect on migratory cell polarization.

## Sequestration of polymerization-competent actin in epithelial actin belts explains the inhibition of migratory cell polarization by myosin-II

Since myosin is an actin-based mechanochemical ATPase[11], we decided to investigate how activity of myosin is coordinated with the actin cytoskeleton to regulate epithelial cell morphodynamics. Control cells accumulate most of their actin inside peripheral circumferential bundles (epithelial actin belt or ring), which is reflected in the extremely high ratio of F-actin fluorescence in the ring *vs.* the cytoplasm (Fig. 3a). This subcellular distribution of actin mirrors that of active myosin (MRLC-Thr18, Ser19[16]) (Fig. 3b). Consistent with the spatial pattern of both proteins, we determined by laser ablation that actomyosin bundles within the ring are contractile (Supplementary Video 4). After laser ablation, F-actin in the peripheral actomyosin ring recovered with a mean half-time ($\tau_{1/2}$) of 3.0 min (SEM = 0.4 min, n = 10 cells), whereas F-actin in the cytoplasm recovered significantly faster (mean $\tau_{1/2}$ = 10.2 s, SEM = 0.9 s, n = 10 cells; $p < 0.001$, paired samples t-test). However, peripheral F-actin recovered with the kinetics similar to that of cytoplasmic F-actin (mean $\tau_{1/2}$ = 10.0, SEM = 0.8 s, n = 12 cells; $p > 0.5$, two-tailed unpaired Student's t-

test) upon inactivation of myosin with BBS, suggesting that myosin stabilizes actin inside the actomyosin ring.

Acute inhibition of myosin activity with BBS resulted in a reduced ratio of F-actin fluorescence at the cell edge *vs.* the cytoplasm (Fig. 3c, top, first 15 minutes of exposure to the drug). These changes were paralleled by increased levels (1.5-fold change) of G-actin in the cytoplasm as visualized by DNase I staining[17, 18] (Fig. 3c, bottom left). The increase in G-actin levels indicated that F-actin stabilized in the actomyosin ring becomes available for turnover upon myosin inhibition. At later stages (within ~ 40 minutes) of BBS treatment, the cells started accumulating F-actin at the cell edge (Fig. 3c, top), which was accompanied by a small but statistically significant decrease (1.25-fold change) in the levels of cytosolic G-actin (Fig. 3c, bottom left). The latter suggested that the G-actin released upon turnover of F-actin from the actomyosin ring is recycled at the cell edge. Consistent with this conclusion, our experiments on G-actin incorporation *in situ*[19] showed that BBS addition stimulates cells to engage more G-actin into actin networks at the cell edge over time (Fig. 3c, bottom right).

Collectively, these data showed that when myosin activity is suppressed, actin previously "locked" inside the actomyosin ring becomes available for deployment in the processes of actin assembly-disassembly-and-recycling typical for treadmilling actin arrays at the lamellipodium of migrating cells[20]. These actin dynamics were crucial for driving migratory cell polarization upon myosin inactivation, as pharmacological treatments to simultaneously stabilize F-actin and prevent incorporation of G-actin into the existing F-actin network (*via* application of a mixture of jasplakinolide and latrunculin, as described in[21]) in cells pretreated with BBS for 15 minutes, entirely abrogate spontaneous cell polarization (100 % of n = 35 cells).

### Myosin-II-dependent actin immobilization inside peripheral actomyosin bundles suppresses autocatalytic growth of F-actin at the cell edge

At the ultrastructural level, the submembranous F-actin that enables lamellipodial protrusion in migratory polarized cells is known to be organized in a branched fashion[22, 23]. This spatial organization of F-actin is determined by the Arp2/3 protein complex that binds pre-existing growing actin filaments and stimulates the formation of new actin branches[22], thus serving as a specific molecular marker of growing branched actin networks at the light microscope level. Accordingly, we found Arp2/3 primarily concentrated inside submembranous actin meshworks at the protrusive edge of myosin-inhibited cells, but not at the edge of control cells (Fig. 4a). We surmised that preexisting submembranous actin networks in myosin-inhibited cells start utilizing G-actin released upon turnover of actin filaments previously stabilized inside the actomyosin ring. This allows the cells to nucleate more actin filaments at the emerging protrusive edge. The more actin filaments get engaged in the growth at the membrane, the more surfaces will be offered for Arp2/3 to bind preexisting actin filaments and stimulate the formation of new filaments, thus amplifying actin polymerization in an autocatalytic manner[24, 25]. In support of this, we observed that Arp2/3 is not essential for the initial actin enrichment at the plasma membrane seen upon myosin downregulation (Fig. 4b). However, at later stages, Arp2/3 activity appeared to be

crucial for a strong augmentation of the actin enrichment and its transformation into membrane protrusion (Fig. 4c). To see whether the Arp2/3-dependent reinforcement of actin polymerization is implicated in the process of migratory polarization in myosin-inhibited cells, we co-treated cells with BBS and Arp2/3-inhibiting drugs. Such cells displayed diminished membrane protrusivity and a low frequency of spontaneous cell shape polarization compared to cells treated with BBS and inactive control compounds (Fig. 4d, e). These observations suggest that Arp2/3-mediated branching of submembranous actin is required to harness the increased pool of polymerization-competent actin for spontaneous symmetry breaking and motility initiation in myosin-inhibited cells.

## A minimal model for migratory cell polarization

To link the established local mechanisms to global cell-scale morphodynamics, we developed a mathematical model (Supplementary Note), in which we consider cell shape and movement as functions of myosin strength that controls the balance between bundled and branched actin at the cell periphery. The model is based on the following theoretical assumptions and experimental observations: 1) Epithelial cells simultaneously assemble and maintain two major F-actin networks of different organization and dynamics: a small protruding band of branching filaments at the cell periphery and stationary contractile actomyosin bundles forming a cell-scale ring. 2) Consumption of actin by one F-actin network is critical to limit the amount of actin available for the other network[26]. 3) The two actin networks are engaged in local mutual inhibition: a) Peripheral actin gets immobilized inside actomyosin bundles with the rate proportional to myosin strength. b) Growth of the protruding actin filament network at the cell edge is expected to create effective local centripetal flow pushing the actomyosin bundles away from the edge. 4) Local movements of the cell edge affect the inhibitory cross-talk between the networks in two ways: a) If the edge retracts, actomyosin bundles accumulate at the cell boundary compressing branched F-actin into bundles. b) If the edge protrudes, the growing branched filaments keep up with the edge while the actomyosin bundles lag behind. 5) Local network densities determine local cell edge dynamics: branched filaments push the edge outward, while contraction of circumferential bundles pulls the edge inward. The model has the features of a system that describes two species competing for the same resources[27]. As the two actin networks locally compete for the same pool of actin, they cannot co-exist. Rather, one "wins" over the other to ultimately determine the degree of migratory cell polarity.

The model generated a phase diagram of cell migration phenotypes based on two control parameters: i) myosin-dependent rate at which actin gets immobilized in actomyosin bundles; and ii) the rate at which the growing branched actin network locally propels the cell edge and transports actomyosin bundles away from the edge (Fig. 5a). This phase diagram predicted that cells polarize and initiate motility at an intermediary range of myosin activity (Fig. 5a, cells B to C, and Supplementary Video 5), while extreme myosin activity levels (too high or too low) produce nonpolarized cells deficient in migration. When myosin is fully activated, actin immobilization inside circumferential actomyosin bundles inhibits the membrane protrusion all around the cell periphery, resulting in a non-motile cell (Fig. 5a, cell A, Supplementary Fig. 4a, cell F, and Supplementary Video 6). With complete myosin inactivation, actin-based protrusions develop all around the cell and migration cannot be

efficient due to failure of such cells to form a single axis of polarity (Fig. 5a, cell D, Supplementary Fig. 4a, cell E, and Supplementary Video 7). Indeed, we established experimentally that BBS-treated cells polarize efficiently only in the presence of serum in the standard growth medium (Supplementary Fig. 5), which according to recent studies[28] is required to maintain basal levels of actomyosin contractility during cell transitions to amoeboid motility. This suggested that the BBS concentration we use in our experiments inhibits actomyosin contractility partially, and a remaining myosin activity maintained by serum growth factors is essential for cell polarization. To test this in a more specific way, we modulated myosin activity with different concentrations of BBS at standard conditions (in the presence of serum). Our BBS dose-response experiments showed that both the degree of cell polarity and motility initiation frequency are insensitive to low concentrations of the drug (5–10 μM), but reach maximal values at an intermediate range of BBS concentrations (20–60 μM). High concentrations of the inhibitor (80–100 μM), which inactivate the cellular pool of myosin completely[29], decreased frequency of motility initiation events. Such cells switched to irregular shapes by extending protrusions in different directions simultaneously, which precluded polarized cell movements (Fig. 5b). Thus, our experimental results are in agreement with predicted cell behaviors.

### Spatial segregation among branched and bundled actin networks establishes cell-scale polarity

Our theoretical and experimental data suggested that untreated stationary cells possess relatively high basal levels of myosin activity and that intermediary ranges of myosin activity are optimal for migratory cell polarization in this system. Stochastic simulations at intermediary ranges of myosin activity revealed that once actin bundling gets randomly suppressed along a significant part of the cell boundary, branched filaments at this part of the boundary will emerge and start pushing forward the cell membrane, leaving remnants of bundled filaments behind. This predicted that the local cell edge displacement should allow preferential accumulation of remaining actomyosin bundles behind the protrusive edge thus establishing spatial asymmetries in the actin cytoskeleton (Fig. 6a and Supplementary Note). To test this mechanism, we decided to inhibit cell edge displacement without directly interfering with the growth of F-actin and see how it affects F-actin polarization triggered by partial myosin inactivation in cells. In order to suppress cell edge motion, we placed cells inside microfabricated cavities of a size and shape comparable to those of single cells (a circle with a diameter of 30 μm). In these conditions, cell edge displacement gets limited by the spatial constrains (Fig. 6a). BBS-treated cells on regular glass surfaces exhibited clear spatial separation between the branched actin mesh at the emerging front and remnants of actin bundles lagging behind during early stages of polarization (Fig. 6a). In contrast, cells grown within microfabricated substrates failed to separate branched and bundled actin populations; instead, branched actin starts growing all around the cell boundary, while remaining actin bundles get accumulated inside the cell (Fig. 6a). This supports the hypothesis that cell edge displacement is crucial for initial spatial separation of two distinct actin networks. In an alternative set of experiments, we inhibited cell motility by growing individual cells on circular micropatterns of fibronectin with a diameter of 40 μm, only 10 μm larger than the average cell size (~ 30 μm). In these conditions, cells preserved the ability to change cell shape upon myosin inhibition, however, they failed to generate stable

asymmetry as their motility was restricted by the size of the adhesive micropattern (Supplementary Fig. 6), thus corroborating the model prediction.

## Long-range crosstalk from front to back: Actin growth and retrograde flow transports myosin-II to the back of the cell, maintaining a contractility gradient across the cell

Stochastic simulations showed that fluctuations in the density of actin, intrinsic to the process of actin polymerization, could easily disrupt the initial cell polarity established through the branch-bundle network separation mechanism. Since our experiments demonstrate that myosin-inhibited cells can maintain their migratory polarity over time (Fig. 1b, red curve and Supplementary Video 3), some specific mechanisms should be in place to stabilize cell polarity. F-actin network in motile cells often flows rearward as it polymerizes[30, 31]. In our experiments, we discovered that upon partial myosin inhibition both F-actin and myosin start flowing from the cell front (Fig. 6b). Assuming that the flowing F-actin network transports myosin, but not the other way around, our simulations suggested that actin retrograde flow is a long-range inhibition mechanism (Fig. 6b, Supplementary Fig. 4e): the flow leads to myosin accumulation at the back, where the motor is crucial for contracting actin network and thus limiting its growth.

In agreement with the theoretical predictions, our experiments showed that myosin-inhibited cells at initial stages of symmetry breaking display centripetal flows of actin bundle remnants into the cell interior and increased rates of actin polymerization (Fig. 7a) concomitant with the emergence of retrograde flows of myosin (Fig. 7b and Supplementary Video 8). These myosin flows persist in fully polarized migrating cells and are dependent on actin polymerization, as pharmacological treatments that stabilize the existing F-actin network and prevent new actin polymerization[21] completely arrested the flows (Fig. 7c). The model predicts that myosin should move with the rate and direction similar to that of actin retrograde flow. We triggered cell polarization using Y-27632 and then applied correlational fluorescent speckle microscopy[32] to confirm remarkably similar kinetics and kinematics for actin and myosin flows (see quantification in Fig. 7c).

We further found that the passive rearward transport of myosin results in a front-back gradient of myosin concentrations across the cell with the lowest levels of myosin at the front of the cell and highest at the back (Fig. 7d). To determine whether this gradient of myosin distribution is indicative of spatial differences in contractility across the cell, we ablated the actin network with a pulsed laser beam at the front and the back of actomyosin-relaxed cells. Indeed, by comparing recoil velocity of the cytoskeleton after laser cut[33], we observed a five-fold increase in contractility from the front to the back (Supplementary Fig. 7). To equilibrate the spatial distribution of myosin across the cell and check how it affects cell polarity, we slowed down myosin flow by acutely inhibiting Arp2/3-dependent actin polymerization. In these conditions, cells started to gradually lose an asymmetric geometry, which is reflected in the increase of cell shape circularity index over time in most of the analyzed cases (80%, n = 15) (Fig. 7d). Thus, local depletion of myosin from the leading edge by actin retrograde flows reinforces global front-back asymmetry. When we examined F-actin structure and dynamics in Arp2/3-inhibited cells upon BBS treatment, we found that such cells assemble linear actin cables throughout the entire cell periphery (Supplementary

Fig. 8). Previous reports show that this F-actin pattern emerges in Arp2/3-inactivated cells due to random formation of peripheral actin cables by formins at the expense of Arp2/3-dependent branched actin meshworks normally focused at the leading cell edge[26, 34, 35]. Thus, in addition to the mechanisms we describe in this work, spatial restriction of actin assembly by different actin-nucleating factors could impact cell polarization.

### The role of reduced contractility in epithelial biology

To test the generality of the proposed model, we first partially inactivated myosin in two other epithelial cell lines (canine kidney (MDCK-2) and fetal bovine tracheal (FBT) epithelial cells). These cells, similar to IAR-2 epithelial cells, display peripheral actomyosin rings. Upon treatment with BBS (25 μM), MDCK-2 and FBT cells lost their actomyosin rings and acquired migratory polarized shapes with distinctive actin mesh-rich pseudopodia at the front (Fig. 8a), therefore confirming the phenotype of myosin-inhibited IAR-2 cells (Fig. 1a and Fig. 4a). Next, we tested whether epithelial cell shape polarization takes place in conditions that physically and chemically mimic *in vivo* epithelial microenvironments. We cultured IAR-2 cells within three-dimensional (3D) Matrigel™ basement membrane matrices. The cells grown in control conditions displayed perfectly symmetric spherical morphology (Fig. 8b). However, myosin inhibition in these cells resulted in an invasive phenotype exhibiting cell dissemination into the basement membrane matrix. Such cells acquired elongated shapes with pronounced actin-filled protrusions and inverted orientation of epithelial polarity, such that the Golgi apparatus becomes misoriented towards the basement membrane matrix, which is a distinctive feature of motile mesenchymal cells displaying anteroposterior polarity[36, 37] (Fig. 8b–d). A similar behavior was observed in a classical model of epithelial 3D morphogenesis, non-tumorigenic human mammary gland epithelial cells (MCF-10A) (Fig. 8c). To see whether the epithelial cell shape polarization phenotype in 3D is also dependent on branched polymerization of actin filaments, we co-treated myosin-inactivated IAR-2 cells growing in 3D matrices with Arp2/3-inhibiting drugs. We found that the elongated invasive morphology of myosin-inhibited cells was strongly dependent on Arp2/3-mediated branched polymerization of F-actin (Fig. 8e). Thus, we established that actomyosin contractility restrains migratory polarization of epithelial cells in 3D microenvironments, and that shifting the balance between actin bundling and branching is sufficient to trigger transitions between discrete cell shapes both in 2D and 3D conditions (Fig. 8f).

## Discussion

Competition for a limiting resource is most commonly attributed to ecological communities[38]. However, recent works demonstrate that competitive interactions also apply at the molecular level inside a living cell. It has been shown that Arp2/3-mediated F-actin meshworks compete for G-actin with formin- or Ena/VASP-assembled actin polymers to regulate size and structure of the bulk F-actin cytoskeleton in both fission yeast and animal tissue cells[26, 39, 40]. Our findings provide a functional application for similar processes, in which competition among Arp2/3- and myosin-dependent F-actin networks defines a mechanism for cell polarization and motility initiation. At the core of this mechanism is the ability of the actin-based motor myosin-II to immobilize actin inside cortical actomyosin

bundles and thus make it unavailable for deployment in the process of dendritic growth. We show that non-tumorigenic epithelial cells are inherently motile and rely on the dendritic actin growth at the cell edge to propel themselves; however, this property is normally inhibited by myosin activity. This is because the actin machinery in epithelial cells engages primarily in the assembly of contractile actomyosin bundles and is thus unavailable to form polarized protrusions required for motility. The key for the proposed mechanism to work is the ability of myosin to stabilize actin in contractile actomyosin structures, which is consistent with results of previous functional and biochemical studies[41–45]. Furthermore, different types of non-motile or slow moving cells are known to exhibit a large pool of stabilized F-actin, while fast moving cells are characterized by significantly enhanced F-actin turnover rates and a lower pool of stable F-actin[46]. The mechanism might explain why direct or indirect myosin-II inactivation stimulates the formation of polarized actin-rich protrusions and promotes cell migration in a variety of cell types and experimental settings[8, 9, 47–51].

In order to reach and colonize a distant place in the organism, epithelial cells in a developing embryo or during carcinogenesis employ a large arsenal of migration modes[52, 53]. Resent work on various cell types has identified specific mechanisms and conditions required for myosin-dependent polarization and amoeboid motility when cells are in high contractility mode[15, 28]. Our research explores the other end of the spectrum – low contractility regimes – and contributes to understanding of the intrinsic mechanisms behind transitions of epithelial cells to mesenchymal-like phenotypes. We found that decreasing contractility below a critical threshold level of myosin activity is sufficient to switch epithelial cells from a stationary non-polarized mode to a stably polarized migratory state. We show that this stable polarization is maintained by the autocatalytic growth of the branched actin network at the front and by a long-range crosstalk from the front to the back in which continuous membrane protrusion at the front produces actin retrograde flow, transporting myosin to the back. Consistent with these observations, recent findings demonstrate that the actin flow-driven assembly of stable myosin gradients across the cell is a generic property of cells undergoing polarized migration[54]. We demonstrate that the transition of epithelial cells to a stably polarized migratory state is reversible. These data coupled to our minimal mathematical model suggest that the observed transition does not require an elaborate genetic program, but rather occurs as a simple mechanical switch triggered by decreased contractility. Since levels of myosin-dependent contractility are reversibly modulated by physico-chemical properties of the extracellular environment[11], cells *in vivo* can utilize the myosin-dependent switch to choose between different morphodynamic modes depending on environmental conditions.

## Methods

### Cell culture

Normal rat liver (IAR-2), canine kidney (MDCK-2), and fetal bovine tracheal (FBT) epithelial cells were maintained in DMEM/F12 supplemented with 10% FBS (Invitrogen) at 37°C and 5% $CO_2$. Cell lines were tested for mycoplasma contamination using MycoScope™ PCR Mycoplasma Detection Kit (Genlantis). For experiments, cells were

plated at a low confluence (10–20%) on $22 \times 22$–mm #1.5 acid-washed coverslips with no pre-coating for 24 h before experimental manipulations. In experiments for Supplementary Fig. 4, cells were plated on plasma-treated glass coverslips coated with either fibronectin (Millipore), poly-L-lysine (Merck KGaA), BSA (Sigma-Aldrich), or poly-L-lysine-PEG copolymer (SuSoS AG).

### Transfection procedure, expression vectors, and siRNA oligonucleotides

Cells were transfected with plasmid DNA using Lipofectamine™ LTX reagent (Invitrogen) transiently or stably, according to manufacturer's protocol. For RNA interference experiments, cells were transfected with siRNA oligonucleotides using Lipofectamine® RNAiMAX reagent (Invitrogen), according to manufacturer's protocol.

The following expression vectors were used for plasmid DNA transfections: empty vector pEGFP-C1 (Clontech); pCMX-*myc*- p160[ROCK](wt) and pCMX-*myc*-p160[ROCK]("kinase-dead"/kd)[55]; pcDNA3-EGFP-cofilin(wt), pcDNA3-EGFP-cofilin(S3D), and pcDNA3-EGFP-cofilin(S3A)[56]; pEGFP-Par3(wt), pEGFP-Par3(T833D), and pEGFP-Par3(T833A)[57]; pEGFP-Myosin-IIA and pEGFP-Myosin-IIAN93K27[10]; Addgene plasmids: 13719 pcDNA3-EGFP-Rac1(wt), 13720 pcDNA3-EGFP-Rac1(Q61L), and 13721 pcDNA3-EGFP-Rac1(T17N)[58]; 12599 pcDNA3-EGFP-Cdc42(wt), 12600 pcDNA3-EGFP-Cdc42(Q61L), and 12601 pcDNA3-EGFP-Cdc42(T17N)[59]; 12965 pcDNA3-EGFP-RhoA-wt, 12968 pcDNA3-EGFP-RhoA-Q63L, and 12967 pcDNA3-EGFP-RhoA-T19N[60]; 20671 pHJ320/EGFP-Moesin-wt, 20677 pHJ322/EGFP-Moesin-T558D, and 20676 pHJ321/EGFP-Moesin-T558A[61]; and 35680 pEGFP-MRLC1-wt, 35682 pEGFP-MRLC1-T18D, S19D, and 35681 pEGFP-MRLC-T18A, S19A[62]. Fluorescent protein expression vectors containing the Lifeact sequence were constructed using N1 (Clontech) cloning vectors where EGFP was replaced with mEmerald (wtGFP with the following mutations: F64L, S65T, S72A, N149K, M153T, I167T, and A206K) or mCherry. To insert the Lifeact sequence, the appropriate N1 cloning vector was digested with NheI and BamHI followed by gel purification. cDNA encoding the Lifeact sequence was obtained from IDT (Coralville, IA):

Lifeact Forward:

CTAGCGCCACCATGGGCGTGGCCGACTTGATCAAGAAGTTCGAGTCCATCT CCAAGGAGGAGGGG

Lifeact Reverse:

GATCCCCCTCCTCCTTGGAGATGGACTCGAACTTCTTGATCAAGTCGGCCAC GCCCATGGTGGCG

The complementary Lifeact cDNA sequences were annealed in TE buffer at a concentration of 50 μM and ligated directly into the NheI-BamHI digested cloning vectors to produce fusions of Lifeact-mEmerald and Lifeact-mCherry.

To knockdown genes encoding major isoforms of nonmuscle myosin-II heavy chains in rat epithelial cells IAR-2, cells were transfected with nontargeting siRNA (control) or validated ON-TARGETplus SMARTpool siRNA reagents (Dharmacon) targeting rat-specific *Myh9* (myosin-II A isoform) mRNA (cat. # L-095070-02-0005) or rat-specific *Myh10* (myosin-II

B isoform) mRNA (cat. # L-098035-02-0005). Cells were analyzed 72 h post-transfection using standard Western blot or immunofluorescent analysis protocols. Based on quantitative densitometry of proteins, myosin-II A and myosin-II B knockdown efficiency was estimated as $84.7 \pm 2.5\%$ and $93.7 \pm 1.2\%$ respectively (3 repeats).

### Drug treatments

The following pharmacological inhibitors were used: 25 μM myosin-II inhibitor blebbistatin (Toronto Research Chemicals), 10 μM ROCK inhibitor Y-27632 (EMD), 1 μg/mL Rho inhibitor I (cell permeable C3 Transferase from *Clostridium botulinum*) (Cytoskeleton), 50 μM Cdc42 inhibitor ML 141 (Tocris Bioscience), 50 μM Rac1 inhibitor NSC 23766 (Tocris Bioscience), 0.5 μg/mL microtubule-depolymerizing drug colcemid (Sigma-Aldrich), 0.5 μM actin-stabilizing toxin jasplakinolide (Sigma-Aldrich), 5 μM actin-disrupting drug latrunculin B (Calbiochem) in combination with 8 μM jasplakinolide (a part of the JLY mixture[21]), 25 μM Arp2/3 inhibitors and nonspecific compounds CK-666, -869, and CK-689, -312 (Calbiochem), 35 μM formin FH2 domain inhibitor SMIFH2 (Calbiochem), 5 μg/mL vesicular transport inhibitor brefeldin A (Sigma-Aldrich), 0.5 μM pan-class I PI3K inhibitor BKM120 (Cellagen Technology), 10 μM PTEN inhibitor SF1670 (Cellagen Technology), and 25 μg/ml phosphopeptide activator of PI3K, PDGFR[740]Y-P (Tocris Bioscience). Growth medium was supplemented with 1% DMSO (vol/vol) (Sigma-Aldrich) in control experiments.

### Antibodies and immunofluorescence microscopy

The following antibodies were used: anti-myc tag antibody (clone 4A6), Alexa Fluor® 488 conjugate, #16-224 (Millipore), anti-β-actin antibody (clone EP1123Y) #04-1116 (Millipore), anti-myosin-II regulatory light chain 2/MRLC antibody #3674 (Cell Signaling Technology), anti-Arp2 component of the Arp2/3 protein complex antibody #ab47654 (Abcam), anti-nonmuscle myosin heavy chain II A #ab55456 (Abcam), anti-nonmuscle myosin heavy chain II B #PRB-445P (Covance), anti-Golgi marker GM130 antibody #558712 (BD Pharmingen), and anti-GAPDH antibody #ab9483 (Abcam). Directed against the species of primary antibodies, Alexa Fluor® 488- and Alexa Fluor® 568-conjugated IgG antibodies (Molecular Probes) were used as secondary antibodies. IRDye® and VRDye™ secondary antibodies (LI-COR) were used for Western blotting. Primary and secondary antibodies for immunofluorescence microscopy were used in 1:100 and 1:300 dilutions, respectively. Primary and secondary antibodies for Western blotting were used in 1:1,000 and 1:3,000 dilutions, respectively. F-actin was visualized using Alexa Fluor® 488- or Alexa Fluor® 568-conjugated phalloidin (Molecular Probes). Cells were rinsed with warm (37°C) PBS, fixed in 3% PFA/PBS for 15 minutes at 37°C, permeabilized with 0.5% Triton X-100 for 5 minutes, and blocked with 3% BSA/PBS for 30 minutes at room temperature. Primary and secondary antibodies were diluted using 3% BSA/PBS. Incubation with antibodies, washing and mounting steps were performed according to standard protocols. Samples were imaged using Yokogawa spinning disk confocal system on a Nikon Ti inverted microscope equipped with a 100× Plan Apo NA 1.4 objective lens. Optical sections along Z-axis were collected with a step size of 0.2 μm, using the Nikon Ti internal focus motor. Z-series were displayed as maximum Z-projections.

### Western blotting

Cells were collected and resuspended in Laemmli buffer. Proteins were separated using sodium dodecyl sulfate polyacrylamide gel electrophoresis (SDS–PAGE) and transferred onto PVDF membranes. After incubation with primary and secondary antibodies, the membranes were visualized using Odyssey® CLx Infrared Imaging System (LI-COR). To estimate protein levels and compare them between different samples, protein bands were quantified by densitometric scanning using ImageJ software (NIH, http://rsb.info.nih.gov/ij/index.html). Multiple dilutions of cell extract were analyzed to ensure that the Western signal was linear within the analyzed range for each protein probed.

### G-actin incorporation *in situ* for the localization of barbed ends of actin filaments

To localize and quantify the relative number of polymerization-competent free barbed ends of actin filaments, live cells treated with 25 μM BBS at different time points were briefly permeabilized with 0.25 mg/ml saponin in the presence of 0.5 μM actin purified from rabbit skeletal muscle and conjugated with an activated ester of Rhodamine (Cytoskeleton). After the incorporation of extracellular Rhodamine-actin into the intracellular F-actin network, cells were fixed and stained with Fluorescein-phalloidin to visualize total actin polymer as previously described[19]. The incorporation of newly polymerized actin was then assayed using Rhodamine/Fluorescein ratio-imaging.

### Measuring levels of cytoplasmic G-actin

To assess the levels of G-actin in the cytoplasm, the DNase I/phalloidin staining method was used[17, 18]. Briefly, cells treated with 25 μM BBS at different time points were fixed in 4% formaldehyde (EM grade) with 0.32 M sucrose in the cytoskeleton buffer (10 mM MES, 138 mM KCl, 3 mM MgCl2, 4 mM EDTA, pH 6.1) for 10 min at 37°C. After permeabilization followed by blocking with 3% BSA/PBS, the samples were incubated with 0.3 μM Alexa Fluor® 488-DNaseI and 1:2000 Alexa Fluor® 568-conjugated phalloidin (Molecular Probes). Confocal z-stacks upon subtraction of the background fluorescence were used to measure total integrated fluorescence of DNaseI and phalloidin in individual cells. To avoid changes in G-actin levels associated with cell size heterogeneity, DNaseI and phalloidin fluorescence levels were normalized per cell size. In our experiments, an increase in G-actin levels (DNaseI fluorescence) was always associated with a decrease in F-actin levels (phalloidin fluorescence).

### Live-cell imaging

Cells were plated on glass-bottomed 35-mm dishes (Fluordishes). Phenol red-free DMEM/F-12 media supplemented with 10% FBS (Invitrogen), 10 mM lactate, and OxyFluor™ (Oxyrase) was used during image acquisition, with a layer of mineral oil on top of the media to prevent evaporation. Time-lapse series were collected with a Yokogawa spinning disk confocal system on a Nikon Ti inverted microscope equipped with 37°C, 5% CO2 incubation chamber, 100× Plan Apo NA 1.4 objective lens, solid state lasers for 491nm (100mW) and 561nm (200mW) excitation, and the Perfect Focus System for continuous maintenance of focus. Images were acquired with a Hamamatsu ORCA-AG cooled CCD

camera controlled by MetaMorph 7.7 software (Molecular Devices). Image acquisition details are specified in figure legends.

### Cortical laser ablation (COLA)

Cells were grown on No. 1.5 coverslips and mounted in a 20/20 Technologies Bionomic microscope stage heated chamber warmed to 37°C. Phenol red-free DMEM/F-12 media supplemented with 25 mM Hepes (pH 7.2), 10% FBS (Invitrogen), 10 mM lactate, and OxyFluor™ (Oxyrase) was used during image acquisition, with a layer of mineral oil on top of the media to prevent evaporation. Images were collected on a Nikon Ti-E inverted microscope equipped with a 100× Plan Apo NA 1.4 objective lens and a Prior Proscan II motorized stage (Rockland, MA). The Nikon Perfect Focus System was engaged to maintain a continuous plane of focus. An EXFO X-cite XL-120 epi-fluorescence light source was used for illumination of mEmerald, which was exited with a 480/40 excitation filter and collected with a 505 nm dichroic mirror and 535/50 emission filter from Chroma (Bellows Falls, VT). For laser ablation experiments, a N2 pulsed dye-tunable Micropoint System tuned to 553 nm with MetaMorph controlled galvos for beam positioning was used (Photonics Instruments, St. Charles, IL). Live-cell time-lapse data series were acquired using a Hamamatsu ORCA R2 cooled CCD camera controlled by MetaMorph 7.7 software.

### Microfabricated tools for restricting cell motility and controlling cell shape

Microfabricated substrates of different configurations (microchannels with nanofabricated walls or circular/linear stamps of fibronectin interspaced by non-adhesive areas) were obtained from CYTOO, France.

### 3D Matrigel™ cell culture

MCF-10A cells were cultured as described (http://brugge.med.harvard.edu/protocols). Wells of an 8-well glass chamber slide (Becton Dickson) were coated with Matrigel™ (BD Biosciences). 5,000 cells were counted and mixed with cold MatrigelTM. The mixture was overlaid on top of Matrigel™ contained within each well of the glass chamber slide, allowed to solidify at 37°C, and standard growth media was then added to the cells. After 24–48 h, 3D cultures were fixed with 3.7% PFA/PBS, blocked and stained with 5% BSA, 5% FBS, 5 μg/ml DAPI and 5 U/ml Alexa Fluor® 488-phalloidin. Confocal Z-series were acquired with a 1-μm step size, using a Nikon C1si point scanning confocal microscope equipped with a Plan Fluor multi-immersion 20× 0.75 NA lens. MetaMorph 7.7 software was used for 3D reconstruction of the acquired stacks.

### Quantitative image analysis

Quantitative COLA: Positions of laser-ablated ends of F-actin structure were tracked from a kymograph of a COLA time-lapse movie. The kymographs were constructed using a custom code in Matlab 8.1 software (MathWorks). To enhance the retracting edges of the F-actin structure, stack images were added with 10% of Laplacian-of-Gaussian-filtered images. Edge velocity was calculated by the slopes of regression line of 3 consecutive data points in time-position data.

Cell morphometry: ImageJ software (NIH, http://rsb.info.nih.gov/ij/index.html) was used to acquire binary images of F-actin stained cells and automatically trace cell outlines for measurements of cell surface area (A) and perimeter (P). Circularity ($4\pi(A/P^2)$) was calculated as a normalized ratio of A to P, with a value of 1 representing a perfect circle and a value close to 0 representing more elliptical or elongated surfaces. Aspect ratio (AR) was calculated as a ratio of major cell axis length to minor cell axis length, automatically determined by ImageJ software. An AR value of 1 corresponds to a highly symmetric object.

Membrane protrusivity analysis: Protrusivity was defined as a distance of a cell edge from an average protrusion-retraction cycle. Edge velocities and persistence time at each protrusion/retraction phase of live mEmerald-LifeAct-expressing cells were determined using a custom-written software package[63]. The obtained parameters were averaged. The mean velocities and persistence time were used to calculate the average edge displacement ($d_p$) as $d_p = v_p t_p - v_r t_r$, where $v_p$ is a protrusion velocity, $t_p$ is a protrusion persistence time, $v_r$ is a retraction velocity, and $t_r$ is a retraction persistence time.

Actin/myosin-II flow analysis: MRLC patches were tracked using time-integrated cross-correlation tracking[64] with 3 frames of the time window for evidence accumulation and templates of 11×11 pixels (1pixel = 72 nm). Grid points with 3-pixel spacing were used to track motions of myosin-II. The tracking was validated using standard kymographic analysis; results obtained with these two methods were highly consistent. Centripetal flow of actin bundles was analyzed using the Kymograph function in MetaMorph 7.7 software. Manual kymographic analysis or automated quantitative fluorescent speckle microscopy (qFSM)[65] tools were applied to analyze the retrograde actin flow in lamellipodial regions of cells expressing low levels of Lifeact. The actin polymerization rate was calculated as the sum of the retrograde actin flow and the forward protrusion at the leading edge. To quantitatively characterize the degree of coupling between actin and myosin flows in the same cell, the technique of correlational fluorescent speckle microscopy[32] was employed. The direction coupling score (DCS) was measured by $cos\theta$ ($\theta$: the angle between myosin-II and F-actin displacement vectors within a pair). A score of 1 defines two vectors with identical directionality and a score of -1 defines two vectors that point in opposite directions. The velocity magnitude coupling score (VMCS) is the ratio between the magnitude of the coupled components of F-actin and myosin-II speckle motions, minimizing the influence of random fluctuations. A detailed description of VMCS is provided by Hu *et al.*[32].

### Statistics and reproducibility of experiments

Unless stated otherwise, statistical significance was determined by two-tailed unpaired Student's *t*-test after confirming that the data met appropriate assumptions (normality, homogenous variance and independent sampling). Statistical data are presented as average ± either SEM or SD. Sample size (n) and p-value are specified in the text of the paper or figure legends. Samples in most cases were defined as the number of cells counted/examined within multiple different fields of view on the same dish/slide, and thus represent data from a single sample within a single experiment, that are representative of at least three additional independently conducted experiments..

## Supplementary Material

Refer to Web version on PubMed Central for supplementary material.

## Acknowledgements

## References

1. Nieto MA. Epithelial plasticity: a common theme in embryonic and cancer cells. Science. 2013; 342:1234850. [PubMed: 24202173]

2. Muthuswamy SK, Xue B. Cell polarity as a regulator of cancer cell behavior plasticity. Annu. Rev. Cell Dev. Biol. 2012; 28:599–625. [PubMed: 22881459]

3. Hall A. Rho GTPases and the actin cytoskeleton. Science. 1998; 279:509–514. [PubMed: 9438836]

4. Bakal C, Aach J, Church G, Perrimon N. Quantitative morphological signatures define local signaling networks regulating cell morphology. Science. 2007; 316:1753–1756. [PubMed: 17588932]

5. Sahai E, Marshall CJ. Differing modes of tumour cell invasion have distinct requirements for Rho/ROCK signalling and extracellular proteolysis. Nat. Cell Biol. 2003; 8:711–719. [PubMed: 12844144]

6. Sanz-Moreno V, et al. Rac activation and inactivation control plasticity of tumor cell movement. Cell. 2008; 135:510–523. [PubMed: 18984162]

7. Croft DR, Olson MF. Regulating the conversion between rounded and elongated modes of cancer cell movement. Cancer Cell. 2008; 14:349–351. [PubMed: 18977323]

8. Even-Ram S, et al. Myosin IIA regulates cell motility and actomyosin-microtubule crosstalk. Nat. Cell Biol. 2007; 3:299–309. [PubMed: 17310241]

9. Schramek D, et al. Direct in vivo RNAi screen unveils myosin IIa as a tumor suppressor of squamous cell carcinomas. Science. 2014; 343:309–313. [PubMed: 24436421]

10. Vicente-Manzanares M, Zareno J, Whitmore L, Choi CK, Horwitz AF. Regulation of protrusion, adhesion dynamics, and polarity by myosins IIA and IIB in migrating cells. J. Cell Biol. 2007; 176:573–580. [PubMed: 17312025]

11. Vicente-Manzanares M, Ma X, Adelstein RS, Horwitz AR. Non-muscle myosin II takes centre stage in cell adhesion and migration. Nat. Rev. Mol. Cell Biol. 2009; 10:778–790. [PubMed: 19851336]

12. Gupton SL, Waterman-Storer CM. Spatiotemporal feedback between actomyosin and focal-adhesion systems optimizes rapid cell migration. Cell. 2006; 125:1361–1374. [PubMed: 16814721]

13. Wu X, Kodama A, Fuchs E. ACF7 regulates cytoskeletal-focal adhesion dynamics and migration and has ATPase activity. Cell. 2008; 135:137–148. [PubMed: 18854161]

14. Barnhart E, Lee KC, Allen GM, Theriot JA, Mogilner A. Balance between cell-substrate adhesion and myosin contraction determines the frequency of motility initiation in fish keratocytes. Proc. Natl Acad. Sci. USA. 2015; 112:5045–5050. [PubMed: 25848042]

15. Liu YJ, et al. Confinement and low adhesion induce fast amoeboid migration of slow mesenchymal cells. Cell. 2015; 160:659–672. [PubMed: 25679760]

16. Watanabe T, Hosoya H, Yonemura S. Regulation of myosin II dynamics by phosphorylation and dephosphorylation of its light chain in epithelial cells. Mol. Biol. Cell. 2007; 18:605–616. [PubMed: 17151359]

17. Cramer LP, Briggs LJ, Dawe HR. Use of fluorescently labelled deoxyribonuclease I to spatially measure G-actin levels in migrating and non-migrating cells. Cell Motil. Cytoskeleton. 2002; 51:27–38. [PubMed: 11810694]

18. Connelly JT, et al. Actin and serum response factor transduce physical cues from the microenvironment to regulate epidermal stem cell fate decisions. Nat. Cell Biol. 2010; 12:711–718. [PubMed: 20581838]

19. Symons MH, Mitchison TJ. Control of actin polymerization in live and permeabilized fibroblasts. J. Cell Biol. 1991; 114:503–513. [PubMed: 1860882]

20. Pollard TD, Blanchoin L, Mullins RD. Actin dynamics. J. Cell Sci. 2001; 114:3–4. [PubMed: 11112680]

21. Peng GE, Wilson SR, Weiner OD. A pharmacological cocktail for arresting actin dynamics in living cells. Mol. Biol. Cell. 2011; 22:3986–3994. [PubMed: 21880897]

22. Mullins RD, Heuser JA, Pollard TD. The interaction of Arp2/3 complex with actin: nucleation, high affinity pointed end capping, and formation of branching networks of filaments. Proc. Natl. Acad. Sci. USA. 1998; 95:6181–6186. [PubMed: 9600938]

23. Yang C, Svitkina T. Visualizing branched actin filaments in lamellipodia by electron tomography. Nat. Cell Biol. 2011; 13:1012–1013. [PubMed: 21892140]

24. Sambeth R, Baumgaertner A. Autocatalytic polymerization generates persistent random walk of crawling cells. Phys. Rev. Lett. 2001; 86:5196–5199. [PubMed: 11384455]

25. Carlsson AE. Dendritic actin filament nucleation causes traveling waves and patches. Phys. Rev. Lett. 2010; 104:228102. [PubMed: 20867207]

26. Burke TA, et al. Homeostatic actin cytoskeleton networks are regulated by assembly factor competition for monomers. Curr. Biol. 2014; 24:579–585. [PubMed: 24560576]

27. Edelstein-Keshet, L. Mathematical Models in Biology. Philadelphia, PA: SIAM; 2005.

28. Ruprecht V, et al. Cortical contractility triggers a stochastic switch to fast amoeboid cell motility. Cell. 2015; 160:673–685. [PubMed: 25679761]

29. Shutova M, Yang C, Vasiliev JM, Svitkina T. Functions of nonmuscle myosin II in assembly of the cellular contractile system. PLoS One. 2012; 7:e40814. [PubMed: 22808267]

30. Henson JH, et al. Two components of actin-based retrograde flow in sea urchin coelomocytes. Mol. Biol. Cell. 1999; 10:4075–4090. [PubMed: 10588644]

31. Ponti A, Machacek M, Gupton SL, Waterman-Storer CM, Danuser G. Two distinct actin networks drive the protrusion of migrating cells. Science. 2004; 305:1782–1786. [PubMed: 15375270]

32. Hu K, Ji L, Applegate KT, Danuser G, Waterman-Storer CM. Differential transmission of actin motion within focal adhesions. Science. 2007; 315:111–115. [PubMed: 17204653]

33. Mayer M, Depken M, Bois JS, Jülicher F, Grill SW. Anisotropies in cortical tension reveal the physical basis of polarizing cortical flows. Nature. 2010; 467:617–621. [PubMed: 20852613]

34. Koestler SA, et al. Arp2/3 complex is essential for actin network treadmilling as well as for targeting of capping protein and cofilin. Mol. Biol. Cell. 2012; 24:2861–2875. [PubMed: 23885122]

35. Henson JH, et al. Arp2/3 complex inhibition radically alters lamellipodial actin architecture, suspended cell shape, and the cell spreading process. Mol. Biol. Cell. 2015; 26:887–900. [PubMed: 25568343]

36. Kupfer A, Louvard D, Singer SJ. Polarization of the Golgi apparatus and the microtubule-organizing center in cultured fibroblasts at the edge of an experimental wound. Proc. Natl. Acad Sci. USA. 1982; 79:2603–2607. [PubMed: 7045867]

37. Bryant DM, Mostov KE. From cells to organs: building polarized tissue. Nat. Rev. Mol. Cell Biol. 2008; 9:887–901. [PubMed: 18946477]

38. Gause, GF. The struggle for existence. Baltimore, MD: Williams & Wilkins; 1934.

39. Suarez C, et al. Profilin regulates F-actin network homeostasis by favoring formin over Arp2/3 complex. Dev. Cell. 2015; 32:43–53. [PubMed: 25543282]

40. Rotty JD, et al. Profilin-1 serves as a gatekeeper for actin assembly by Arp2/3-dependent and -independent pathways. Dev. Cell. 2015; 32:54–67. [PubMed: 25543281]

41. Engl W, Arasi B, Yap LL, Thiery JP, Viasnoff V. Actin dynamics modulate mechanosensitive immobilization of E-cadherin at adherens junctions. Nat. Cell Biol. 2014; 16:587–594. [PubMed: 24859003]

42. Wu SK, et al. Cortical F-actin stabilization generates apical-lateral patterns of junctional contractility that integrate cells into epithelia. Nat. Cell Biol. 2014; 16:167–178. [PubMed: 24413434]

43. Wiggan O, Shaw AE, DeLuca JG, Bamburg JR. ADF/cofilin regulates actomyosin assembly through competitive inhibition of myosin II binding to F-actin. Dev. Cell. 2012; 22:530–543. [PubMed: 22421043]

44. Elam WA, Kang H, De La Cruz EM. Competitive displacement of cofilin can promote actin filament severing. Biochem. Biophys. Res. Commun. 2013; 438:728–731. [PubMed: 23911787]

45. Hayakawa K, Tatsumi H, Sokabe M. Actin filaments function as a tension sensor by tension-dependent binding of cofilin to the filament. J. Cell Biol. 2011; 195:721–727. [PubMed: 22123860]

46. McGrath JL, Osborn EA, Tardy YS, Dewey CF Jr, Hartwig JH. Regulation of the actin cycle in vivo by actin filament severing. Proc. Natl Acad. Sci. USA. 2000; 97:6532–6537. [PubMed: 10823888]

47. Omelchenko T, Vasiliev JM, Gelfand IM, Feder HH, Bonder EM. Mechanisms of polarization of the shape of fibroblasts and epitheliocytes: Separation of the roles of microtubules and Rho-dependent actin-myosin contractility. Proc. Natl Acad. Sci. USA. 2002; 99:10452–10457. [PubMed: 12149446]

48. Omelchenko T, Vasiliev JM, Gelfand IM, Feder HH, Bonder EM. Rho-dependent formation of epithelial "leader" cells during wound healing. Proc. Natl Acad. Sci. USA. 2003; 100:10788–10793. [PubMed: 12960404]

49. Wang HR, et al. Regulation of cell polarity and protrusion formation by targeting RhoA for degradation. Science. 2003; 302:1775–1779. [PubMed: 14657501]

50. Asokan SB, et al. Mesenchymal chemotaxis requires selective inactivation of myosin II at the leading edge via a noncanonical PLCγ/PKCα pathway. Dev. Cell. 2014; 31:747–760. [PubMed: 25482883]

51. Lou SS, Diz-Muñoz A, Weiner OD, Fletcher DA, Theriot JA. Myosin light chain kinase regulates cell polarization independently of membrane tension or Rho kinase. J. Cell Biol. 2015; 209:275–288. [PubMed: 25918227]

52. Lämmermann T, Sixt M. Mechanical modes of 'amoeboid' cell migration. Curr. Opin. Cell Biol. 2009; 21:636–644. [PubMed: 19523798]

53. Friedl P, Alexander S. Cancer invasion and the microenvironment: plasticity and reciprocity. Cell. 2011; 147:992–1009. [PubMed: 22118458]

54. Maiuri P, et al. Actin flows mediate a universal coupling between cell speed and cell persistence. Cell. 2015; 161:374–386. [PubMed: 25799384]

## References for the Methods section

55. Ishizaki T, et al. p160ROCK, a Rho-associated coiled-coil forming protein kinase, works downstream of Rho and induces focal adhesions. FEBS Lett. 1997; 404:118–124. [PubMed: 9119047]

56. Pontrello CG, et al. Cofilin under control of β-arrestin-2 in NMDA-dependent dendritic spine plasticity, long-term depression (LTD), and learning. Proc. Natl. Acad. Sci. USA. 2012; 109:E442–E451. [PubMed: 22308427]

57. Nakayama M, et al. Rho-kinase phosphorylates PAR-3 and disrupts PAR complex formation. Dev. Cell. 2008; 14:205–215. [PubMed: 18267089]

58. Kraynov VS, et al. Localized Rac activation dynamics visualized in living cells. Science. 2000; 290:333–337. [PubMed: 11030651]

59. Nalbant P, Hodgson L, Kraynov V, Toutchkine A, Hahn KM. Activation of endogenous Cdc42 visualized in living cells. Science. 2004; 305:1615–1619. [PubMed: 15361624]

60. Subauste MC, et al. Rho family proteins modulate rapid apoptosis induced by cytotoxic T lymphocytes and Fas. J. Biol. Chem. 2000; 275:9725–9733. [PubMed: 10734125]

61. Hao JJ, et al. Phospholipase C-mediated hydrolysis of PIP2 releases ERM proteins from lymphocyte membrane. J. Cell Biol. 2009; 184:451–462. [PubMed: 19204146]

62. Beach JR, Licate LS, Crish JF, Egelhoff TT. Analysis of the role of Ser1/Ser2/Thr9 phosphorylation on myosin II assembly and function in live cells. BMC Cell Biol. 2011; 12:52. [PubMed: 22136066]

63. Machacek M, Danuser G. Morphodynamic profiling of protrusion phenotypes. Biophys. J. 2006; 90:1439–1452. [PubMed: 16326902]

64. Ji L, Danuser G. Tracking quasi-stationary flow of weak fluorescent signals by adaptive multi-frame correlation. J. Microsc. 2005; 220:150–167. [PubMed: 16363999]

65. Mendoza MC, Besson S, Danuser G. Quantitative fluorescent speckle microscopy (qFSM) to measure actin dynamics. Curr. Protoc. Cytom. 2012; Chapter 2(Unit 2.18)
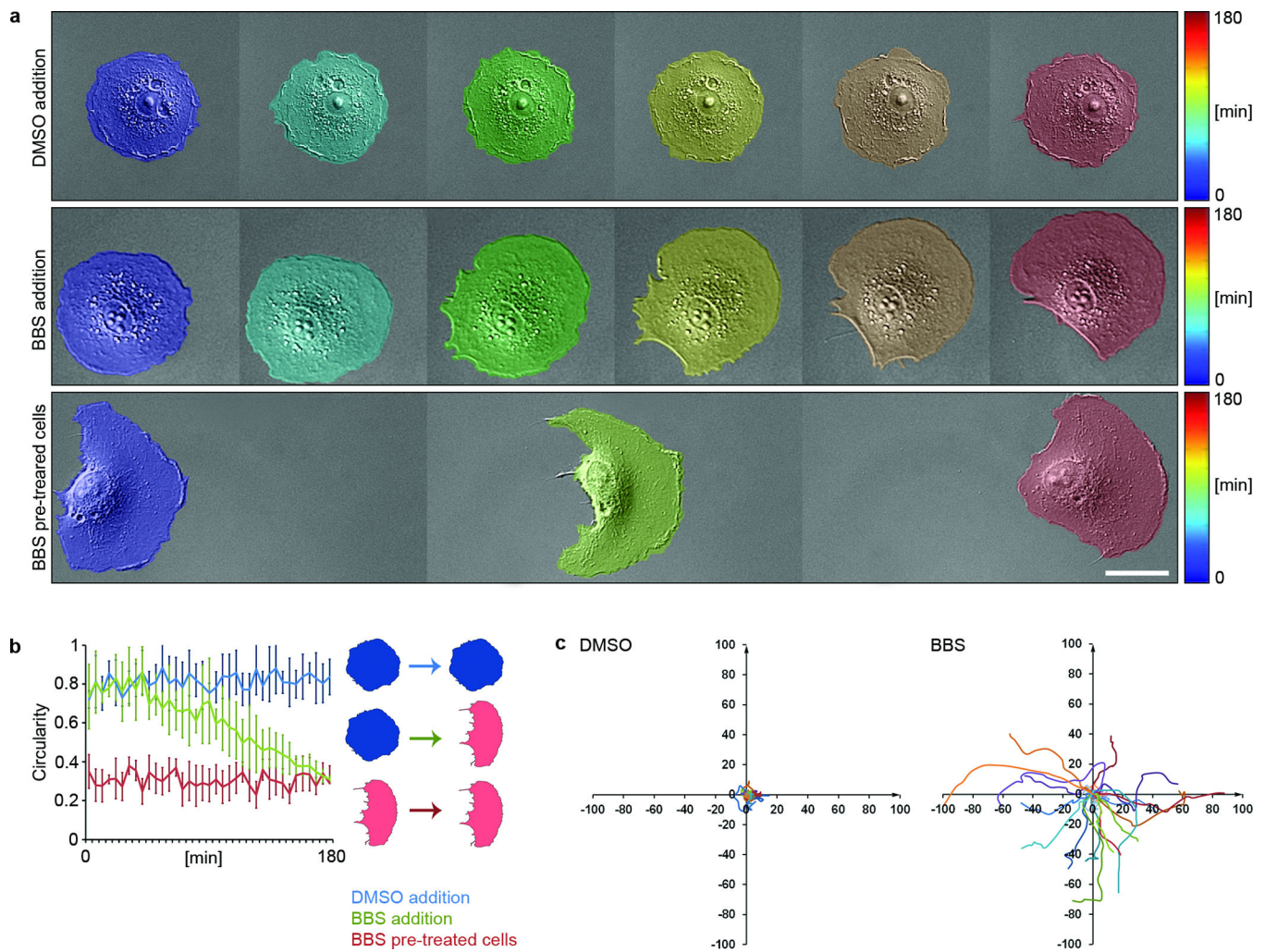
**Figure 1. Acute inhibition of myosin-II activity results in spontaneous symmetry breaking and motility initiation in single epithelial cells**

**a**, Representative video sequences of control cells (DMSO addition), cells after acute exposure to a myosin-II inhibitor (BBS addition), and cells several hours of post-exposure to the inhibitor (BBS pre-treated cells). Scale bar, 20 μm.

**b**, Cell shape circularity index ($4\pi[Area/Perimeter2]$) over time in single live cells at different experimental conditions. High circularity and its persistence over time is a morphodynamic signature of stationary, unpolarized cells. Low circularity is a trait of migratory polarized cells. The decrease in the circularity index over time reflects a cell polarization event. Relatively large standard deviation for the circularity index over time in the BBS addition case is associated with an asynchrony of polarization events between individual cells on the same glass (n = 50 cells per each experimental condition; Mean ± SD).

**c**, Individual cells several hours of post-exposure to BBS display dramatically increased random migration. Trajectories of cell centroids (20 per each condition) of DMSO or BBS-pretreated cells tracked over 3 hours are shown.
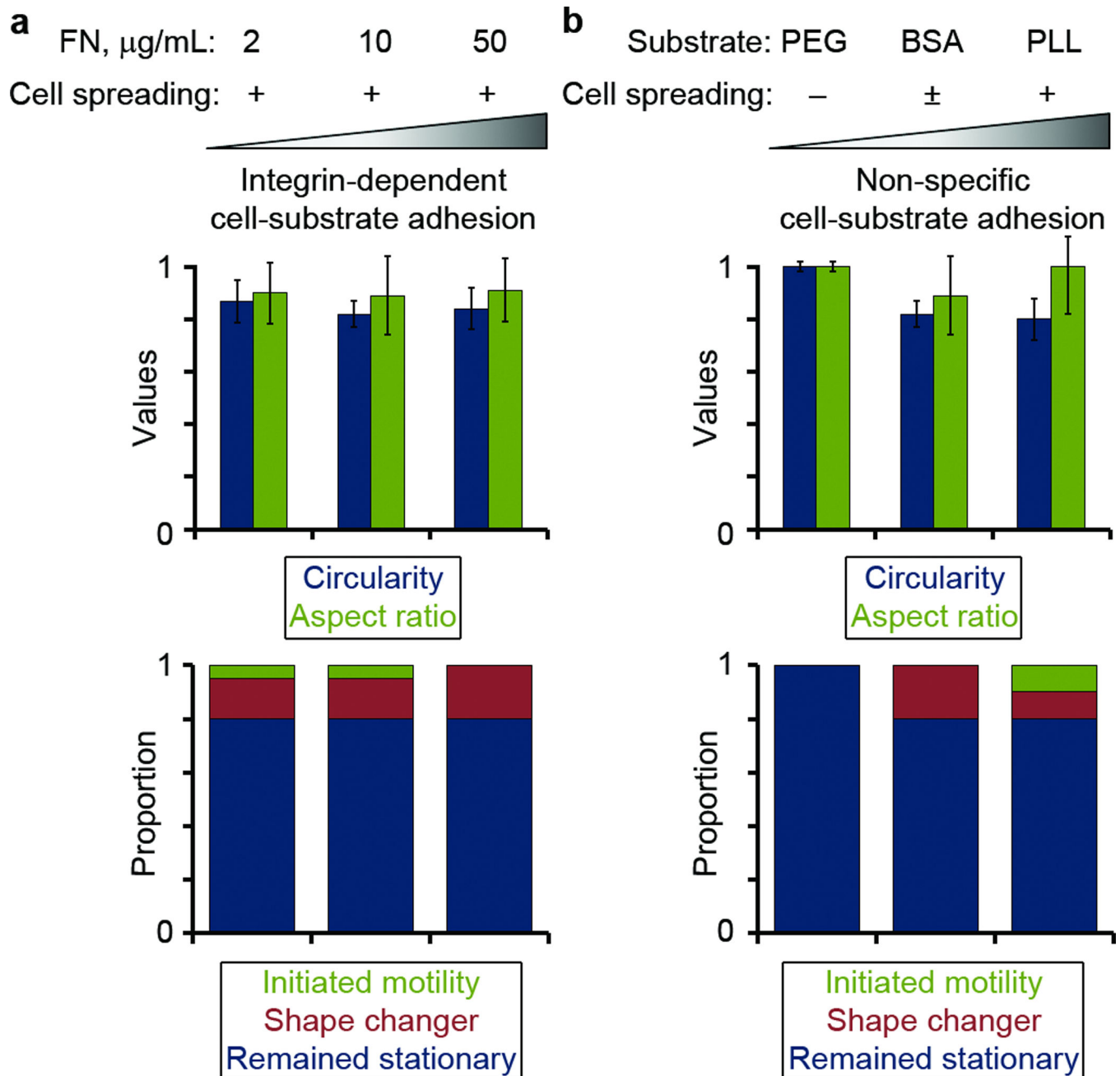
**Figure 2. Modulating cell-substrate adhesion strength *per se* is insufficient to trigger spontaneous symmetry breaking and motility initiation in epithelial cells with intact myosin-II activity**

**a**, Shape descriptors (n = 120 cells per each experimental condition, Mean ± SEM; compared to DMSO-treated cells on glass (Supplementary Fig. 1c), p-values for each of these conditions are > 0.5, two-tailed unpaired Student's t-test) and motility initiation frequency (n = 50 cells per each experimental condition) in pharmacologically untreated epithelial cells plated onto dishes pre-coated with fibronectin (FN) at low (2 μg/mL), intermediate (10 μg/mL), or high (50 μg/mL) concentrations.

**b**, Shape descriptors (n = 120 cells per each experimental condition, Mean ± SEM; compared to DMSO-treated cells on glass (Supplementary Fig. 1c), p-values for each of

these conditions are > 0.5, two-tailed unpaired Student's t-test) and motility initiation frequency (n = 50 cells per each experimental condition) in pharmacologically untreated epithelial cells plated onto dishes pre-coated with 0.2 mg/mL polyethylene glycol (PEG), 50 mg/mL bovine serum albumin (BSA), or 1 mg/mL poly-L-lysine (PLL).
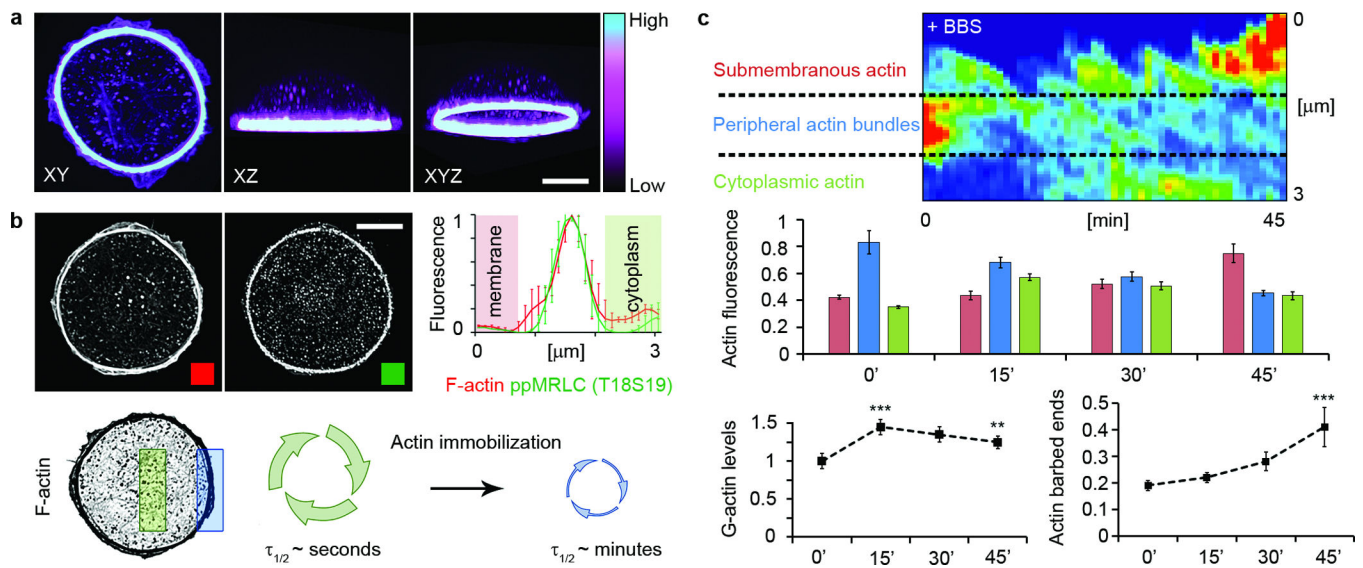
**Figure 3. Myosin-II activity suppresses actin polymerization at the cell edge by immobilizing actin inside peripheral actomyosin bundles**

**a**, Optical sectioning of a fixed stationary epithelial cell stained for F-actin (Rhodamine-phalloidin). The color scale indicates levels of F-actin fluorescence intensity. Scale bar, 10 μm.

**b**, Maximum intensity projections of F-actin and endogenous diphosphorylated myosin-II regulatory light chain (ppMRLC (Thr18/Ser19)) in a fixed stationary epithelial cell. The linescan shows normalized average fluorescence intensity of F-actin (red) and diphosphorylated MRLC (green) along a profile (1 pixel across) pointing from the cell edge to the cytoplasm (n = 95 cells; Mean ± SEM). Both F-actin and diphosphorylated MRLC are concentrated in the cortical actin ring but largely absent from the cytoplasm, where actin turns over significantly faster compared to the cortical ring. Scale bar, 10 μm.

**c**, Dynamic redistribution pattern of actin at the cell periphery in response to acute inhibition of myosin-II activity. Top, a representative kymograph and statistical analysis (n = 35 cells; Mean ± SEM) of local F-actin fluorescence (mCherry-Lifeact) intensity at the membrane, the actin ring, and the cytoplasm monitored in live cells immediately upon addition of BBS. Hot colors on the kymograph represent high levels of F-actin fluorescence, while cool colors are low F-actin fluorescence levels. Bottom left, retrospective analysis of endogenous cytoplasmic G-actin fluorescence levels (a.u., normalized values) at different time points upon addition of BBS (n = 40 cells per each time point; Mean ± SEM; ***p < 0.001 – comparison between 0' and 15' of BBS exposure, **p < 0.01 – comparison between 15' and 45' of BBS exposure, two-tailed unpaired Student's t-test). Bottom right, fraction of submembranous actin barbed (growing) ends (fluorescence intensity ratio of newly incorporated actin monomers *vs.* pre-existing actin polymer) at different time points upon addition of BBS (n = 18 cells per each time point; Mean ± SEM; ***p < 0.001 – comparison between 0' and 45' of BBS exposure, two-tailed unpaired Student's t-test).
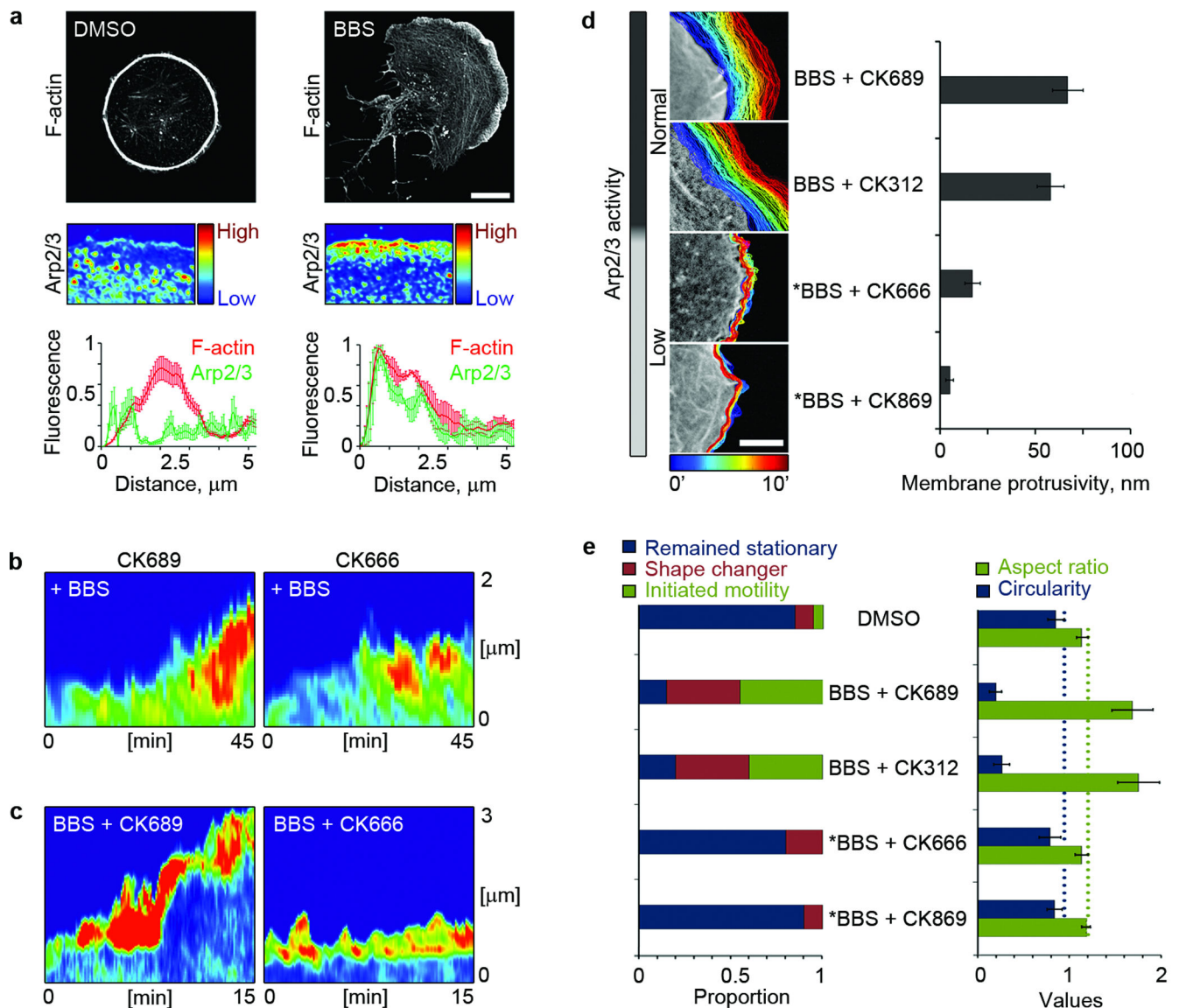
**Figure 4. The growth of submembranous actin at the edge of myosin-II–inhibited cells is strongly reinforced trough Arp2/3-mediated F-actin branching**

**a**, Phalloidin staining (black and white images) and staining intensity of the cell edge by antibodies recognizing the Arp2 subunit of the Arp2/3 protein complex (pseudocolored images with color intensity scale bars) in cells treated with DMSO or BBS. Scale bar, 10 μm. Linescan, normalized average fluorescence intensity (a.u.) of F-actin and Arp2 along a line pointing from the cell edge to the cell center (n = 50 cells per each experimental condition; Mean ± SEM).

**b**, Representative kymographs of F-actin fluorescence (mCherry-Lifeact) intensity at the cell edge immediately upon addition of BBS to cells pretreated with the nonspecific compound CK-689, or the Arp2/3-inhibiting compound CK-666. Hot colors on the kymograph represent high levels of F-actin fluorescence, while cool colors are low F-actin fluorescence levels.

**c**, Representative kymographs of F-actin fluorescence (mCherry-Lifeact) intensity at the cell edge in cells pretreated with a mixture of BBS and the nonspecific compound CK-689, or BBS and the Arp2/3-inhibiting compound CK-666 for several hours. Hot colors on the kymograph represent high levels of F-actin fluorescence, while cool colors are low F-actin fluorescence levels.

**d**, Cell edge dynamics in cells co-treated with BBS and control, nonspecific compounds (CK-689 and CK-312), or BBS and Arp2/3-inhibiting compounds (CK-666 and CK-869) (n = 15 cells per each experimental condition; Mean ± SEM; *p < 0.001, two-tailed unpaired Student's t-test). The representative images of the cell edge dynamics show color-coded outlines of the cell edge. Color scale, time in minutes. Scale bar, 3 μm.

**e**, Left, motility initiation frequency of stationary cells within 4 hours after addition of BBS and control, nonspecific compounds (CK-689 and CK-312), or BBS and Arp2/3-inhibiting compounds (CK-666 and CK-869) (n = 50 cells per each experimental condition). Right, shape descriptors measured in cells after 3 hours of incubation with BBS and control, nonspecific compounds (CK-689 and CK-312), or BBS and Arp2/3-inhibiting compounds (CK-666 and CK-869) (n = 150 cells per each experimental condition; Mean ± SEM; *p < 0.001, two-tailed unpaired Student's t-test).
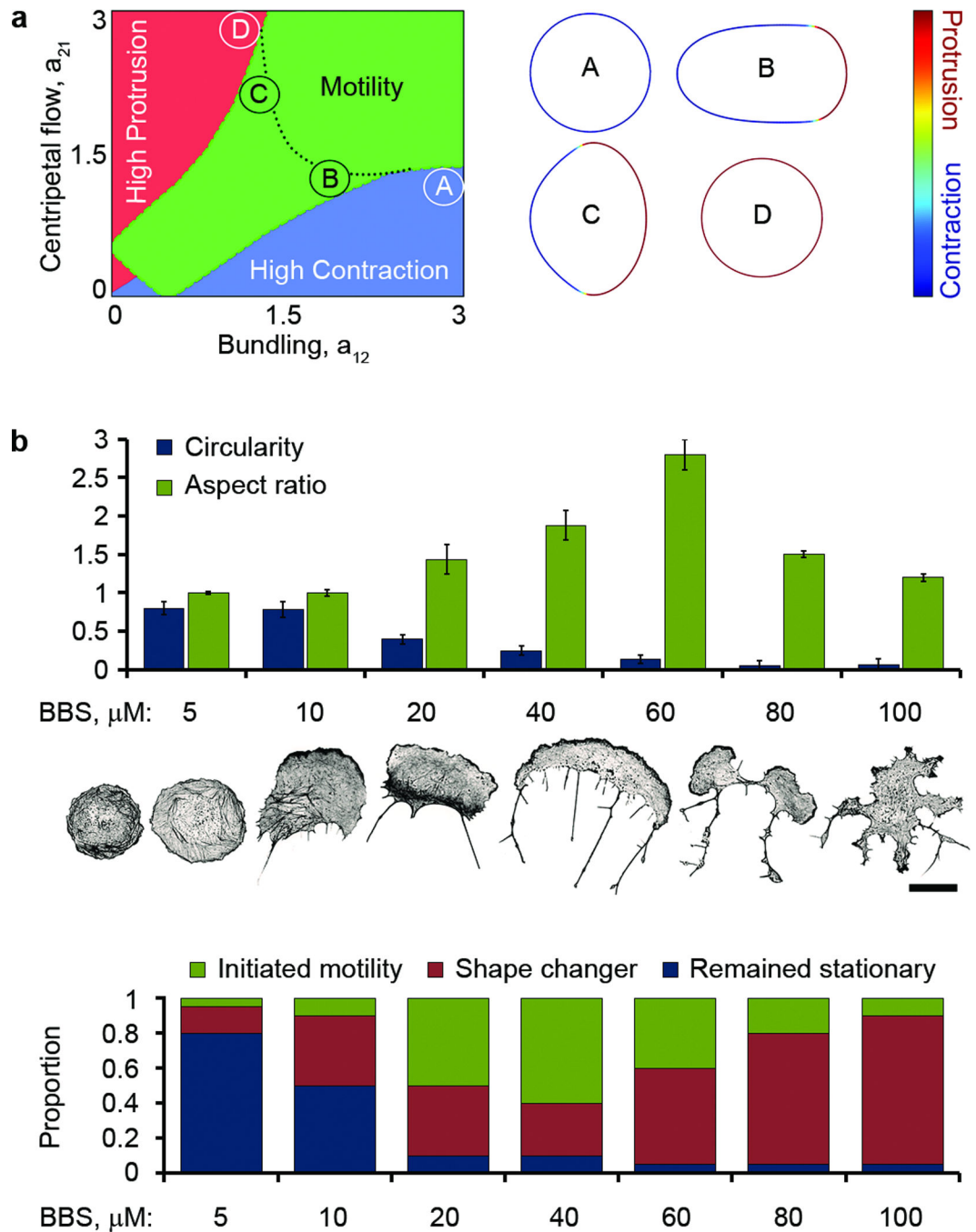
**Figure 5. Mathematical model for migratory cell polarization based on the mass balance between actomyosin bundle formation and branched actin growth coupled to F-actin retrograde flow**

**a**, Motility phase diagram as a function of the bundling rate ($a_{12}$) and centripetal flow rate ($a_{21}$). The control cell corresponds to the high bundling rate (proportional to the myosin strength) and low centripetal flow rate (Cell A [$a_{12} = 3$, $a_{21} = 1.2$]). In this state, a constant high density of bundled actin develops around the periphery of the cell and the cell is symmetric. Inhibition of myosin (Cell B [$a_{12} = 1.8$, $a_{21} = 1.2$]) and enhanced centripetal flow rate (Cell C [$a_{12} = 1.2$, $a_{21} = 1.8$]) can cause the cell to polarize and move. Further

inhibition of myosin and/or increasing centripetal flow rate can abolish cell movement and polarization. In this state (Cell D [$a_{12} = 1.2$, $a_{21} = 3$]), the bundled actin is nearly abolished and the branched actin is constant around the cell periphery creating a propulsive force that is balanced by membrane tension. Dotted line illustrates the path in the parameter space corresponding to gradual weakening of myosin.

**b**, Testing model predictions. Top, shape descriptors measured in cells after 3 hours of incubation with increasing concentrations of BBS (n = 150 cells per each experimental condition; Mean ± SEM). Images of the actin cytoskeleton represent phenotypes of cells treated with different BBS concentrations as indicated on the diagram. Bottom, motility initiation frequency of cells within 4 hours after addition of BBS in different concentrations (n = 50 cells per each experimental condition). Scale bar, 20 μm.
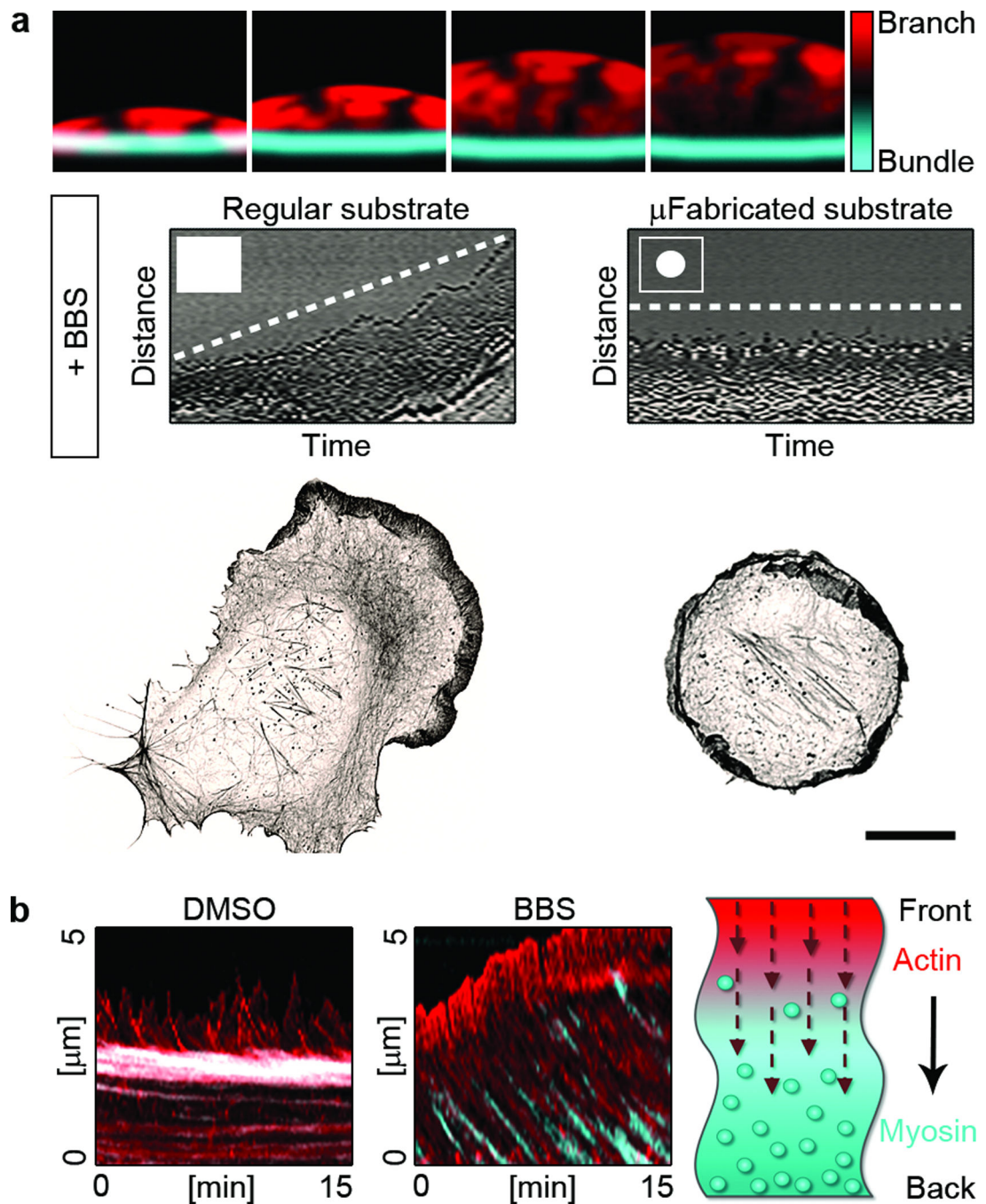
**Figure 6. Low contractility regimes enable spatial segregation among branched and bundled actin networks and facilitate actin-myosin flows**

**a**, Top, abstract representation of the spatial separation between branched and bundled actin populations in myosin-inhibited cells. Middle, representative kymographs of 1.5 hour-long movies of cell edge dynamics upon addition of BBS to cells plated on a regular glass surface *vs.* microfabricated substrate. Bottom, representative images of F-actin distribution (maximum intensity projections) in BBS-pretreated (1.5 hours of exposure to the drug) cells

on a regular glass surface (left) *vs.* cells plated on microfabricated substrates (right). Scale bar, 10 μm.

**b**, Representative kymographs of the edge of live cells expressing F-actin (red) and MRLC (cyan) and pretreated with DMSO or BBS for several hours. The cartoon depicts a possibility of myosin-II's accumulation at the back of the cell *via* actin-myosin retrograde flows.
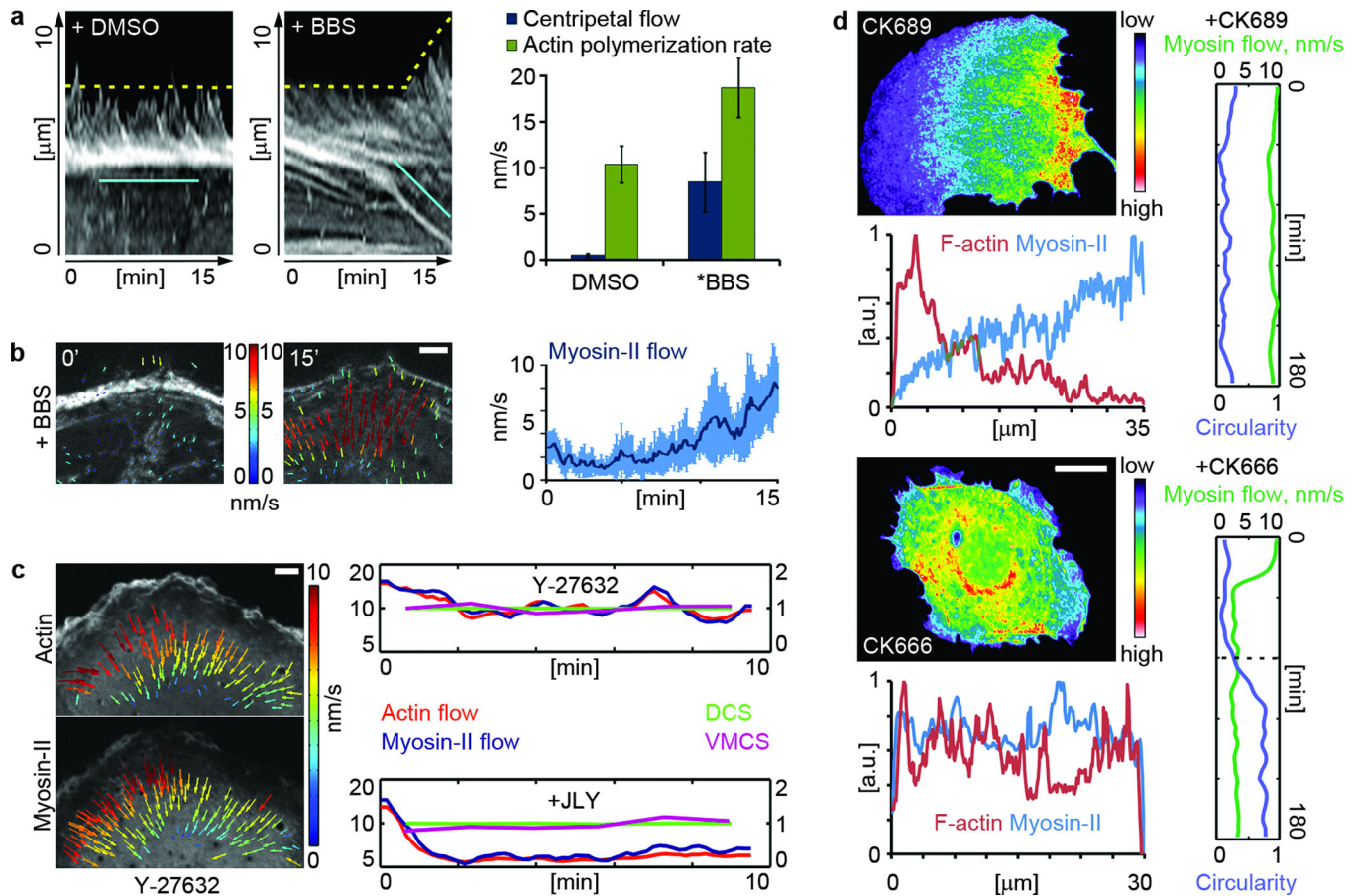
**Figure 7. Experimental validation of model-predicted core motifs that compose the actin/myosin polarity-generating system**

**a**, Left, kymographs of F-actin dynamics upon addition of DMSO or BBS (mCherry-LifeAct-expressing cells). Right, F-actin centripetal flows and actin polymerization rates (n = 20 cells per each condition; Mean ± SEM; *p < 0.001, two-tailed unpaired Student's t-test).

**b**, Left, particle image velocimetry of myosin-II clusters immediately upon addition of BBS (mCherry-MRLC-expressing cells). Color scale, flow velocity. Scale bar, 2 μm. Right, kinetics of myosin-II retrograde flows after the addition of BBS (n = 10 cells; Mean ± SEM).

**c**, Retrograde flows of actin and myosin-II quantified in Y-27632-treated cells, co-expressing GFP-MRLC and mCherry-LifeAct, before and after arresting the F-actin dynamics with a mixture of jasplakinolide and latrunculin on the background of Y-27632 (JLY) (n = 15 cells per each condition). DCS, direction coupling score, a measure of the directional similarities between F-actin and myosin-II motions. VMCS, velocity magnitude coupling score, a measure of relative myosin-II motion along the local F-actin flow axis, thus accounting for both direction and speed. For identical flow fields, both DCS and VMCS are equal to 1. Color scale, flow velocity. Scale bar, 2 μm.

**d**, Staining intensity by an antibody recognizing endogenous MRLC (pseudocolored maximum intensity projections) in cells pre-treated with BBS to induce polarity and subsequently exposed to either the non-specific control compound CK-689 or the Arp2/3

inhibitor CK-666 for 2 hours. Myosin-II in myosin-inhibited cells treated with CK-689 is found at very low levels throughout first 10 μm of the cell front where most of retrograde actin-myosin flow is normally detected. Color scale, staining intensity. Scale bar, 10 μm. Corresponding linescans, normalized average fluorescence intensity of F-actin (red) and MRLC (blue) along a line pointing from the front to the back of the cell. Kinetic profiles, mCherry-MRLC flow velocity (green) and cell shape circularity index (purple) measured at different time points in live cells pre-treated with BBS to induce polarity and subsequently exposed to either CK-689 or CK-666 for 2 hours. Black dotted line, a time point where cells start losing initial polarity.
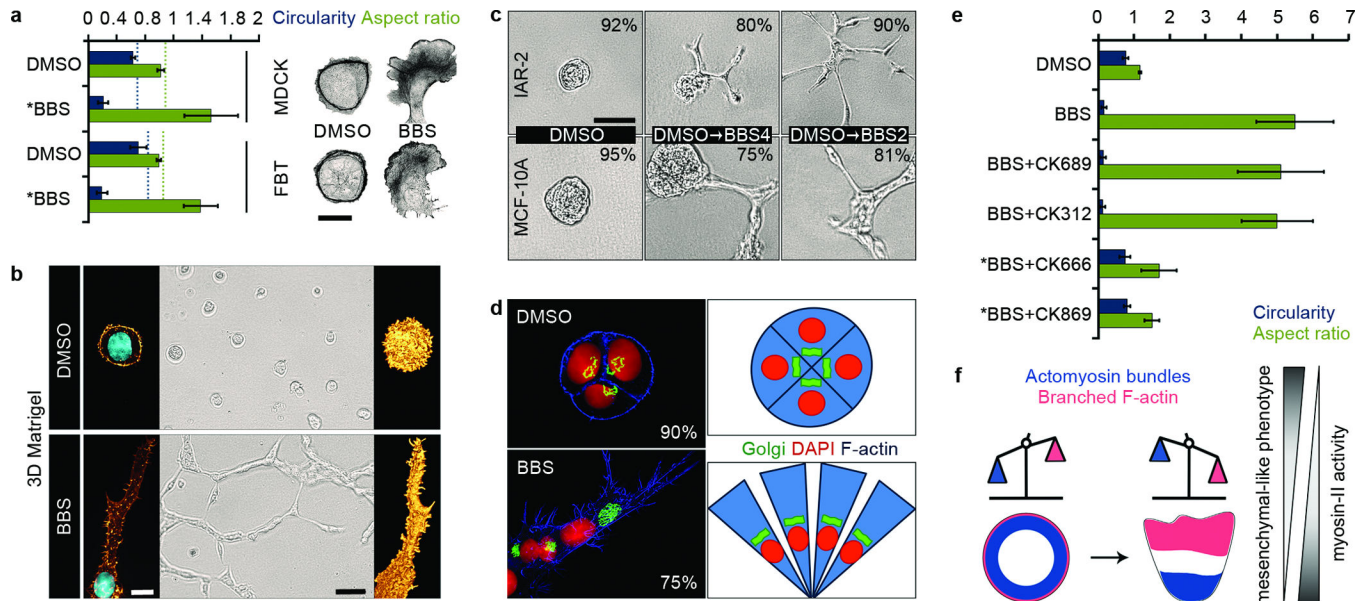
**Figure 8. Testing generality of the actin/myosin polarity-generating mechanism in the context of epithelial biology**

**a**, Shape descriptors in MDCK-2 and FBT epithelial cells (n = 150 cells per each condition; Mean ± SEM; *p < 0.001, two-tailed unpaired Student's t-test). Scale bar, 20 μm.

**b**, Left, nuclear and F-actin staining of single IAR-2 epithelial cells growing in 3D Matrigel. Scale bar, 10 μm. Middle, low-magnification phase-contrast images of single cells in 3D Matrigel. Scale bar, 30 μm. Right, 3D reconstruction of single cell morphology based on optical sectioning of the entire cell volume by confocal microscopy. DMSO, control; BBS, myosin-II inactivation.

**c**, Multicellular spheroid morphogenesis in IAR-2 and MCF-10A epithelial cells growing in 3D Matrigel: DMSO, 4-days old spheroids treated with DMSO for 24 hours; DMSO→BBS4, 3-days old spheroids were treated with DMSO for 24 hours, and on day 4 the medium was changed and BBS was added for 24 hours; DMSO→BBS2, 1-day old spheroids, consisting of 2 to 4 cells, were treated with DMSO for 24 hours, and on day 2 the medium was changed and BBS was added for 48 hours. Percentage of spheroids with representative morphologies (phase contrast images) is indicated; n = 250 spheroids for each data point. Scale bar, 50 μm.

**d**, Internal polarity of individual IAR-2 cells within spheroids assembled in 3D Matrigel: Confocal medial slices of F-actin and the nucleus, as well as maximum intensity projections of the Golgi apparatus, are shown. Percentage of cells with inward (←) and outward (↑) Golgi localization is indicated on images for DMSO and BBS treatment case, respectively; n = 150 cells for each data point. Scale bar, 10 μm.

**e**, Shape descriptors in IAR-2 cells growing in 3D Matrigel and treated with BBS, BBS and nonspecific compounds, or BBS and Arp2/3-inhibiting drugs (n = 180 cells per each condition; Mean ± SEM; *p < 0.001, two-tailed unpaired Student's t-test).

**f**, A simplified model: stationary epithelial cells can be transformed into mesenchymal-like cells upon lowering levels of actomyosin contractility. At low contractility regimes, the

balance between Arp2/3- and myosin-dependent actin networks is shifted toward the growth of branched F-actin crucial for lamellipodial motility.